Available online at www.sciencedirect.com
SCIENCE DIRECT
Applied Catalysis A: General 295 (2005) 40–51
APPLIED CATALYSIS A: GENERAL
www.elsevier.com/locate/apcata

Methane reforming kinetics within a Ni–YSZ SOFC anode support

Ethan S. Hecht [a], Gaurav K. Gupta [b], Huayang Zhu [a], Anthony M. Dean [b], Robert J. Kee [a,*], Luba Maier [c], Olaf Deutschmann [c]

[a] *Engineering Division, Colorado School of Mines, Golden, CO 80401, USA*
[b] *Chemical Engineering Department, Colorado School of Mines, Golden, CO 80401, USA*
[c] *Institute for Chemical Technology and Polymer Chemistry, University of Karlsruhe, Karlsruhe, Germany*

Received 13 July 2005; received in revised form 28 July 2005; accepted 3 August 2005

Abstract

This paper reports experimental and modeling investigations of thermal methane reforming chemistry within porous Ni–YSZ anode materials. Because the reforming chemistry is difficult to observe directly in an operating fuel cell, a specially designed experiment is developed. In the experiment a 0.75 mm-thick anode is sandwiched between two small co-flowing gas channels. One channel represents the fuel channel of a solid-oxide fuel cell (SOFC). The composition in the other channel carries the species that would be produced in an operating fuel cell by the electrochemical charge-transfer reactions in the thin three-phase regions near the interface between the anode and the dense electrolyte membrane (i.e., H_2O and CO_2). Because the anode structure is porous (and there is no dense electrolyte or cathode applied), there is convective and diffusive species flux between the two flow channels. The entire assembly is maintained at approximately 800 °C in a furnace. The results of heterogeneous reforming kinetics are determined by using mass spectrometry to measure the species composition at the outlet of both channels. Experimental results are interpreted using a computational model that incorporates channel gas flow, porous-media transport, and elementary heterogeneous chemical kinetics. The overall objective is to develop quantitative models of non-electrochemical heterogeneous reforming chemistry within a Ni–YSZ anode.

Keywords: Methane reforming; Solid-oxide fuel cell; Heterogeneous kinetics; Reaction mechanism

1. Introduction

An important attribute of solid-oxide fuel cells (SOFC) is the ability to incorporate hydrocarbons into the fuel stream. However, because of deposit-formation problems associated with pure hydrocarbon fuels, practical SOFC systems usually operate on mixtures of H_2, CO, and hydrocarbons [1,2]. The hydrocarbons can be heterogeneously reformed within the anode structure by reacting with steam and CO_2 that are produced by electrochemical charge-transfer processes. There may also be benefits associated with incorporating some oxygen (or air) in the fuel stream, causing internal partial oxidation [3]. Fuel-cell performance depends on the inlet fuel mixture and all the subsequent chemistry within the fuel cell itself. Because hydrocarbon conversion to H_2 and CO greatly affects the charge-transfer chemistry, it is important to understand these thermal reforming processes.

Fig. 1 illustrates the general structure of a Ni–YSZ anode-supported SOFC. The supporting anode is usually on the order of a millimeter thick, with the dense electrolyte and the cathode being on the order of 10 μm thick. In an anode-supported cell, the word ‘‘anode’’ is commonly used with both a broad and narrow meaning. In the narrow, strictly electrochemical, meaning, the anode (negative electrode) is comprised of the Ni particles in the three-phase region (TPR) near the dense electrolyte membrane. Electrons are delivered into the Ni as products of the charge-transfer chemistry. Because the YSZ in the porous Ni–YSZ structure conducts oxygen ions, the thin three-phase region may extend a few microns into the thick porous structure. In the

* Corresponding author. Tel.: +1 303 273 3379.
E-mail address: rjkee@mines.edu (R.J. Kee).

0926-860X/$ – see front matter © 2005 Elsevier B.V. All rights reserved.
doi:10.1016/j.apcata.2005.08.003

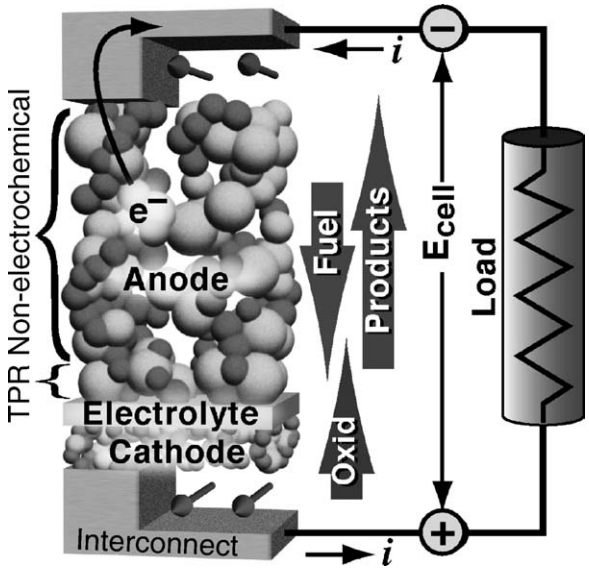

Fig. 1. Illustrated cross-section of an anode-supported SOFC. The relatively thick anode structure is a Ni–YSZ porous ceramic–metallic composite. The dark-colored spheres are meant to represent the Ni with the lighter spheres representing YSZ. To assist visualization, the length scales within the anode structure are distorted. The entire anode structure may be on the order of 1 mm thick, with electrochemical charge-transfer reactions confined to a three-phase region (TPR) that is on the order of 10 μm thick. The particle and pore dimensions are typically on the order of a few microns.

broad meaning, the entire porous Ni–YSZ structure is simply referred to as the anode. Nevertheless, electrochemistry is confined to the very thin three-phase region. Although the physical composition (materials, porosity, microstructure, etc.) may be uniform throughout the anode thickness, the majority of the structure serves non-electrochemical purposes. It serves as a structural support; the Ni is an electron conductor that carries electrons from the charge-transfer region to an interconnect material; and the Ni serves as a reforming catalyst. The work reported in this paper is concerned entirely with the thermal chemistry and transport in the majority of the anode structure where electrochemical effects are completely negligible.

Within the thin three-phase regions of an operating SOFC anode, H_2O and CO_2 are produced via charge-transfer processes. For example, in global terms:

$$H_2(g) + O^{2-}(YSZ) \rightleftharpoons H_2O(g) + 2\,e^-(Ni). \quad (1)$$

In words, gas-phase hydrogen $H_2(g)$ reacts with an oxygen ion emerging from the electrolyte $O^{2-}(YSZ)$ to form steam in the gas phase $H_2O(g)$ and deliver electrons to the anode $e^-(Ni)$. Although the details of the elementary charge-transfer steps remain uncertain, there is no doubt that H_2O and CO_2 are either direct or indirect products of electrochemical charge-transfer reactions. It is also clear that the H_2O and CO_2 must be transported through the porous anode structure away from the TPR and toward the fuel channel.

Within an SOFC anode structure there is ample opportunity for heterogeneous reforming chemistry. Gaseous species are transported via molecular diffusion and pressure-driven flow processes between the anode flow channel and the interface with the dense electrolyte membrane. On their way toward the interface, the hydrocarbons mix with the counter flowing H_2O and CO_2 that are formed as a result of charge-transfer chemistry in the thin TPR. In the presence of a reforming catalyst (e.g., Ni), hydrocarbons may be reformed to produce H_2 and CO. The CO may further react to form CO_2 via water–gas-shift processes. The extent of these processes affects the concentrations of H_2, CO, and hydrocarbons available in the three-phase region, and thus affects details of the charge-transfer processes.

There is considerable evidence that fuel-cell performance can be improved greatly using functionally graded anode structures [4]. Functional variations can include physical structure (e.g., porosity, particle diameter, pore size, and tortuosity) and catalytic activity. Predictive models that quantitatively describe chemical kinetics and gas transport within anode structures are a valuable tools in the optimal design and evaluation of anode structures.

Using specially designed experiments and computational models, the objective of this paper is to develop and validate models that quantitatively describe chemical kinetics and gas transport within anode structures. This paper is specifically concerned with porous ceramic–metallic anodes using nickel and yttria-stabilized zirconia (Ni–YSZ). Further, the paper is specifically concerned with methane as the fuel. Conventional practice in SOFC modeling is to consider that reforming and water–gas-shift processes can be represented as global kinetics processes, or even assumed to be locally equilibrated. The work reported here considers elementary heterogeneous chemical kinetics, coupled with Dusty-Gas representation of the gas transport within the anode.

2. Experimental system

In an operating fuel cell it is difficult to measure directly the heterogeneous chemistry behavior. Moreover, it is essentially impossible to observe the species composition within the very fine (order 1 μm) pore spaces of a ceramic–metallic anode. The interface between the porous anode structure and the dense electrolyte membrane is also completely obscured from direct observation. The purpose of the experiment described here is to create an environment that is much more amenable than the fuel-cell itself for the investigation of thermal chemistry.

A photograph of the experiment is shown in Fig. 2 and a cutaway drawing of the anode assembly is illustrated in Fig. 3. The anode is pressed between two steel fixtures into which 5 cm-long flow channels are machined. The channels have a square cross section of 6.25 mm^2. The anode and

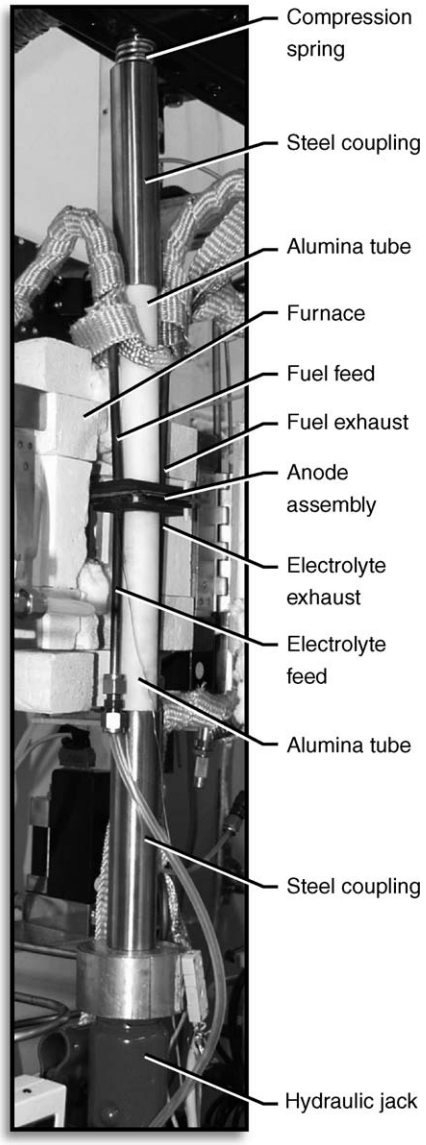

Fig. 2. Photograph of the experiment designed to measure reforming within an SOFC anode. The anode assembly is placed at the center of a temperature-controlled furnace.

fixture assembly are placed within a furnace that maintains the assembly at a uniform high temperature around 800 °C. Thin mica sheets (0.5 mm thick) are used to form a seal between the anode and the steel [5].

A jack at the lower end of the assembly is used to compress a spring at the upper end. The compressive load is carried through 2.5 cm diameter alumina tubes that compress the anode between the channel fixtures. Alumina is used to reduce conductive heat losses from the furnace region. The net compressive pressure to seal the anode between the channels is maintained at about 100 psi (6.9×10^5 Pa).

The upper channel is meant to represent the fuel channel of an SOFC. In the results reported subsequently, it will be fed with a mixture of forming gas (i.e., 3.5% H_2 in Ar) and

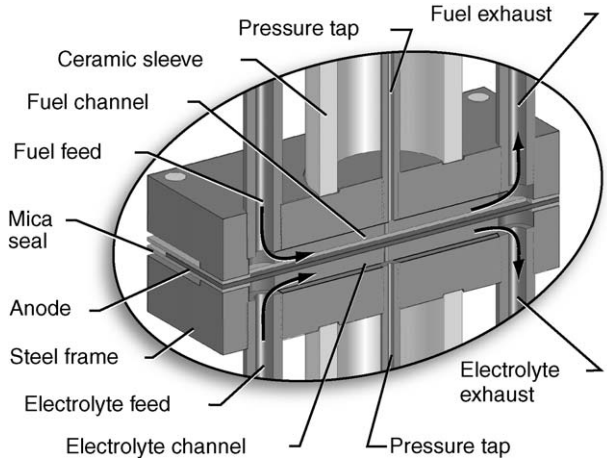

Fig. 3. Cutaway illustration of the anode assembly portion of the experiment.

CH_4. The lower channel is meant to represent the interface between the dense electrolyte and the anode. It is fed with mixtures of forming gas, steam, and CO_2. In an actual fuel cell, the H_2O and CO_2 would be the products of charge-transfer reactions in the three-phase region. The experiment is designed such that the reforming agents (H_2O and CO_2) and the hydrocarbon (CH_4) are being transported through the porous anode in opposite directions. This counter-flow behavior represents the situation in an operating fuel-cell anode structure.

Pressure taps, which are positioned in the center of both channels, are used to monitor and control the pressure difference between the channels. Depending on the fuel and the current density in an SOFC, the pressure difference across the anode can be as high as a few thousand Pascals. The experiment is designed to determine the effects of such pressure differences on the porous-media transport across the anode and hence the reforming chemistry. However, for the experimental conditions reported in this paper, pressure differences as great as 3000 Pa were found to have only a small influence on the reforming rates.

A flow diagram for the system is shown in Fig. 4. Mass flow controllers (Sierra Instruments 810c and Unit Instruments UFC-1100) are used to regulate the inlet-gas flows. On the electrolyte side, inlet gases can flow through a temperature-regulated bubbler where steam is incorporated into the carrier gas. The steam partial pressure is determined from a fit to the vapor–pressure relationship as

$$p_{H_2O} = 133.322 \exp\left(18.3036 - \frac{3816.44}{T - 46.13}\right), \quad (2)$$

where p_{H_2O} is in Pa and T is in K. Between the bubbler and the furnace, heat tape maintains an elevated line temperature to prevent steam condensation. Both the differential pressure and the pressure in the inert channel relative to atmosphere are measured by differential pressure transducers (MKS Instruments Baratron 223b). Needle valves are teed off both

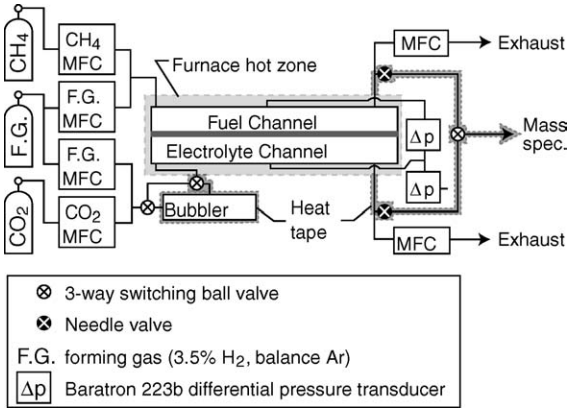

Fig. 4. Flow diagram for the experiment.

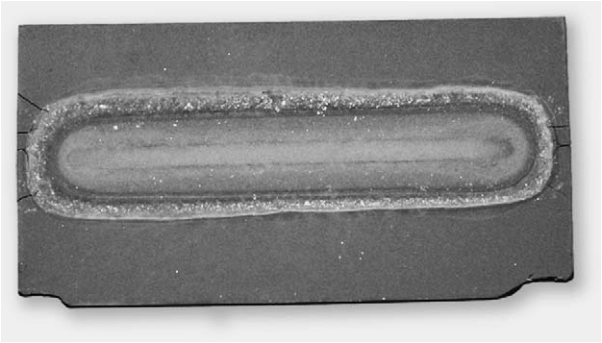

Fig. 5. Photograph of an anode that has been reduced in the area under the flow channels. The regions under the channels and mica are gray in color and the outer regions where NiO is not reduced are green. A faint outline of the relatively narrow channel can be seen in the central area of the reduced region.

exhausts to provide a leak of exhaust gas to the mass spectrometer. These lines are also maintained at high temperature to prevent steam condensation. Downstream of the leak valves, both exhausts flow through mass flow controllers (Unit Instruments UFC-1020). A feedback loop from the pressure transducers regulates these flows and can be used to control the overall pressure above atmosphere as well as the differential pressure across the anode.

Because the anode is porous, there is gas transport between the channels. Methane from the fuel channel reacts heterogeneously on the Ni–YSZ surfaces with H_2O and CO_2 from the lower electrolyte channel to produce H_2 and CO. Flow rates are kept sufficiently high that the chemistry is not equilibrated, and thus the net conversion depends on flow rate. By varying the flow rates chemical kinetics information can be inferred.

A quadrupole mass spectrometer (UTI Instruments model 100C) is used to measure the exhaust composition of both channels. Software was written to identify and fit signals for seven species. At least one peak of the cracking patterns of these molecules is available at a mass-to-charge ratio (m/e) that does not overlap significantly with the other species except for CO, whose cracking pattern overlaps with the CO_2 cracking pattern. CO_2 can be measured accurately at $m/e = 44$. Since the contribution to the signal at $m/e = 28$ due to CO_2 is always a fraction of the signal at $m/e = 44$, this contribution is determined and subtracted from the signal at $m/e = 28$. The only remaining contribution to the signal at 28 is from CO. The nominal m/e values for the species are taken as Ar, 40; H_2O, 18; CH_4, 15; CO_2, 44; CO, 28; O_2, 32; H_2, 2. The methane peak at $m/e = 15$ was used to avoid overlap with a contribution from the H_2O signal. The system was calibrated using gas mixtures of known composition.

3. Ni–YSZ anodes

The anodes used in this work were supplied by ITN Energy Systems (Littleton, CO). They are fabricated by mixing 62.5 g of NiO (Novamet) powder and 37.5 g of 8 mol YSZ (Tosoh) powder with dispersants, binders and water to make a slip. The slip is aged for 3 days and tape cast with a doctor blade. The tapes are approximately 250 μm thick when dry. Four pieces of tape are laminated in a hydraulic press with heated plates (80 °C and 1500 psi). The tapes are then sintered at 1400 °C for 2 h, and subsequently creep-flattened at 1375 °C for 4 h. The final dimensions of the rectangular anodes used in this experiment are approximately 60 mm × 30 mm × 0.75 mm.

The experimental procedure begins by placing the anode-channel assembly within the hot zone of a furnace. Initially the Ni in the Ni–YSZ anode is oxidized as a result of anode-fabrication processes. As the anode is brought to temperature at a rate of 100 °C/h, a flow of forming gas over the anode reduces the nickel oxide to Ni. The anode is considered fully reduced after it has been at temperature under forming gas for more than 24 h.

Fig. 5 shows a photograph of a reduced anode. The region that is between the channels has a gray color, indicating that the NiO has been reduced to Ni. The outer portions of the anode, which are exposed to air, are not reduced and retain the as-fabricated green color. The porosity of the oxidized material is very low, which limits leakage from the channels through the porous anode.

4. Reactive flow model

Fig. 6 illustrates the framework in which the computational model is posed. The model considers plug flow in the fuel- and electrolyte-side channels and reacting porous-media flow within the anode.

4.1. Plug flow in channels

With the small channel dimensions and low flow velocities, the low Reynolds numbers justify a plug-flow approximation. The velocity profile develops rapidly within

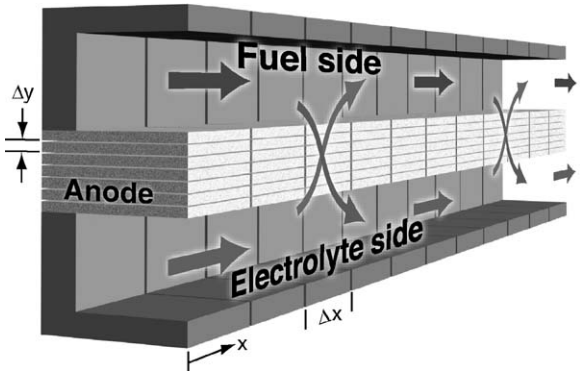

Fig. 6. The computational framework to model transport and chemistry within the anode. Computational solution is accomplished in finite-volume form using an axial mesh interval Δx along the channel length and transverse mesh intervals of Δy through the thickness of the anode.

the channels and using a mean velocity is adequate. Rapid species diffusion across the channel width effectively homogenizes the composition transverse to the flow.

The one-dimensional steady-state channel flows may be described with species continuity and overall continuity equations in each channel as [6–8]:

$$\frac{\mathrm{d}(\rho Y_k u)}{\mathrm{d}x} = \frac{P_\mathrm{e}}{A_\mathrm{c}} J_k W_k, \tag{3}$$

$$\frac{\mathrm{d}(\rho u)}{\mathrm{d}x} = \sum_{k=1}^{K_\mathrm{g}} \frac{P_\mathrm{e}}{A_\mathrm{c}} J_k W_k. \tag{4}$$

The independent variable is the distance along the channel x and the dependent variables are mean channel velocities u and species mass fractions Y_k. Although the pressure p could be determined by solving momentum equations, the pressure variations along a channel are sufficiently small that the pressure is considered a parameter. However, the pressure may be different in the two channels. The temperature is assumed to be uniform at the imposed furnace temperature. The local gas-phase density ρ is determined from a perfect-gas equation of state, involving the pressure, temperature, and species composition. The species molecular weights are represented as W_k.

Because the anode is porous, gases from one channel are free to pass through the anode toward the other channel. Within the anode the gases are free to react heterogeneously, consuming some species and forming others. The gas-phase transport is modeled using a Dusty-Gas model described subsequently. The molar flux of each species entering (or leaving) a channel is represented as J_k. The perimeter P_e is the specific area along the channel wall through which the flux J_k flows. In the experiment here P_e is effectively the width of the anode exposed to the channel flow. The transport and chemistry within the anode couples the two channel flows via the fluxes J_k that enter and exit each channel.

The plug-flow formulation (Eqs. (3) and (4)) neglects gas-phase chemistry, heterogeneous chemistry on the metal channel walls, and stream-wise species diffusion. It should be noted, however, that retaining these effects in the channel model presents no essential difficulties and our software implementation provides the capability to retain these effects when appropriate.

At temperatures around 800 °C and lower, homogeneous methane pyrolysis or reaction with H_2O or CO_2 is very slow. For the short residence times in the experiments here it is very reasonable to neglect the gas-phase chemistry [9]. However, in other circumstances including higher temperatures, higher hydrocarbons, or partial-oxidation conditions, homogeneous chemistry should be retained. Relative to the very high catalyst-surface area within the anode it is reasonable to neglect any heterogeneous chemistry on the stainless-steel channel walls.

Even though the flow velocities in the channels are low, axial species diffusion is negligible under the experimental conditions used here. Although diffusion coefficients can be high for light species like hydrogen, the gradients are low. Even for light species like hydrogen, diffusion velocities are estimated to be on the order of 1 cm/s. With typical convective velocities in the range of 60–180 cm/s, it is reasonable to neglect axial diffusion.

4.2. Reactive porous media

Within the anode, where the pore size is comparable to the molecular mean-free-path length, there is very little probability for gas–gas collisions. Consequently, gas-phase chemistry can be safely neglected. However, it is essential to model gaseous species transport through the pore system and thermal heterogeneous chemistry. The continuity equation for reactive porous-media species transport is written as

$$\nabla \cdot (\mathbf{j}_k) = A_s W_k \dot{s}_k, \quad k = 1, \ldots, K_\mathrm{g}, \tag{5}$$

where $\mathbf{j}_k = W_k \mathbf{J}_k$ are gas-phase mass fluxes, $\mathbf{J}_k$ are mole fluxes, W_k are molecular weights, and A_s is the specific catalyst area (i.e., area per unit volume). The species production rates by heterogeneous chemistry are represented by $\dot{s}_k$. The mass fluxes are evaluated using the Dusty-Gas model (DGM), in which the fluxes are driven by gradients in concentrations and pressure [10].

The DGM can be written as an implicit relationship among the molar concentrations, molar fluxes, concentrations gradients, and the pressure gradient [11,12]:

$$\sum_{\ell \neq k} \frac{[X_\ell]\mathbf{J}_k - [X_k]\mathbf{J}_\ell}{[X_T] D^\mathrm{e}_{k\ell}} + \frac{\mathbf{J}_k}{D^\mathrm{e}_{k,\mathrm{Kn}}} = -\nabla [X_k] - \frac{[X_k]}{D^\mathrm{e}_{k,\mathrm{Kn}}} \frac{B_\mathrm{g}}{\mu} \nabla p. \tag{6}$$

In this relationship $[X_k]$ are the molar concentrations and $[X_T] = p/RT$ is the total molar concentration. The mixture viscosity is given as μ, and $D^\mathrm{e}_{k\ell}$ and $D^\mathrm{e}_{k,\mathrm{Kn}}$ are the effective

molecular binary diffusion coefficients and Knudsen diffusion coefficients.

The effective molecular binary diffusion coefficients in the porous media $D^{e}_{k\ell}$ are related to the ordinary binary diffusion coefficients $D_{k\ell}$ in the bulk phase as

$$D^{e}_{k\ell} = \frac{\phi_g}{\tau_g} D_{k\ell}, \tag{7}$$

where ϕ_g is the porosity and τ_g is the tortuosity [10]. The ordinary binary diffusion coefficients, $D_{k\ell}$, which are determined from kinetic theory, may be evaluated with software such as CHEMKIN [13] or CANTERA [14]. Knudsen diffusion, which occurs due to gas-wall collisions, becomes dominant when the mean-free path of the molecular species is much larger than the pore diameter. The effective Knudsen diffusion coefficient can be expressed as

$$D^{e}_{k,\mathrm{Kn}} = \frac{4}{3} K_g \sqrt{\frac{8RT}{\pi W_k}}, \tag{8}$$

where the Knudsen permeability coefficient $K_g = r_p \phi_g / \tau_g$, and r_p is the average pore radius [10].

Assuming that the porous electrode is formed by closely packed spherical particles with diameter d_p (an idealization), the permeability B_g can be expressed by the Kozeny–Carman relationship [15] as

$$B_g = \frac{\phi_g^3 d_p^2}{72\tau_g (1-\phi_g)^2}. \tag{9}$$

Other porous-media situations have different permeability relationships.

Assuming one-dimensional transport through the thickness of the anode, Eq. (5) is a second-order boundary-value problem. Its solution requires boundary conditions at the interfaces with the two flow channels. Here the boundary conditions are taken to be the gas-phase species compositions in the channels.

4.2.1. Heterogeneous chemistry

In recent years an increasing number of heterogeneous catalysis systems have been successfully described by mechanistic schemes based on molecular behavior at the catalytic surface. For example, this approach has led to a better understanding of three-way catalytic converters [16], syngas production by partial oxidation of methane over Rh [17], and oxidative dehydrogenation of ethane over Pt [18].

Using a mean-field approximation, the species molar-production rates $\dot{s}_k$ depend on the concentrations of the gaseous species and also on the coverages of all surface species, which must be computed self-consistently with the gas-phase species concentrations. At steady state, the net production rates of all surface species must vanish, since transport of surface species over macroscopic distances by surface diffusion is assumed to be negligible. Therefore, the K_g gas-phase continuity equations (i.e., Eq. (5)) are supplemented by the following K_s algebraic equations of the surface species:

$$\dot{s}_k = 0, \quad k = 1, \ldots, K_s. \tag{10}$$

which are functions of the surface-species coverages θ_k and the gas-phase concentrations and temperature.

It is known that Ni can catalyze coke formation from hydrocarbon fuels. However, under the flow conditions reported here, no coking is observed. The experiment is run for days at a time without any degradation in reforming performance. The photograph shown in Fig. 5, which was taken after 5 days of operation, shows no evidence of coking or deposit formation. Several factors may contribute to the deposit-free operation. The methane is relatively dilute in argon and there is always sufficient H_2O or CO_2 available to avoid deposits.

4.3. Computational algorithm

The governing equations are a system of differential–algebraic equations that may be solved computationally [8]. The time-like independent variable is x, the distance along the channels. The plug-flow equations (Eqs. (3) and (4)) are ordinary differential equations coupled to the anode porous-media problem (Eqs. (5) and (10)) by the species fluxes J_k exchanged between the anode and the channels. The porous-media problem is a boundary-value problem in y, the coordinate normal to the channels. The boundary values required for solution are the species compositions in the channels. Computationally, the porous-media problem (having no time-like derivatives) behaves as an algebraic constraint on the plug-flow differential equations.

The solution algorithm used here is a finite-volume method. The channels are divided into cells of length Δx and the anode is divided into cells of height Δy (Fig. 6). For the results shown subsequently the 5 cm long channels have been divided into 200 cells and the anode is divided into 50 cells across its 0.75 mm thickness. Solution requires a few minutes on a personal computer.

5. Heterogeneous reaction mechanism

In the anode application, Ni serves as both a reforming catalyst and an electrical current conductor. Because nickel is used widely as a reforming catalyst there is a great deal of information available about its catalytic behavior. Depending on the actual process (e.g., steam reforming, dry reforming with CO_2, total and partial oxidation) different reaction mechanisms and corresponding kinetic models [19–22] have been proposed. Recently, mechanistic models based on the knowledge about the elementary steps and their energetics have been developed [22–24].

The geometrical layout and support structure of steam reformers or catalytic partial oxidation (CPOX) reactors are usually quite different from that in an SOFC anode.

Steam reforming reactors are usually implemented in packed-bed, porous-foam, or monolith configurations. The ceramic support is usually alumina. An SOFC anode is fabricated as a porous metal–ceramic composite, where the metal, ceramic, and gas phases each occupy roughly 30% of the volume. Although porosity is roughly 30%, the characteristic pore dimensions are typically much smaller (say around 1 μm) than would be typical of a packed-bed or porous-foam reactor. In the SOFC application the ceramic should be an oxygen-ion conductor (e.g., YSZ), which alumina is not. Thus the catalyst-support chemistry may be different with a YSZ support than it is for an alumina support. Moreover there is evidence that the YSZ itself also has catalytic activity for partial oxidation [25].

Table 1 lists a reaction mechanism that we have developed to describe the heterogeneous kinetics within a

Table 1
Heterogeneous reaction mechanism for CH_4 reforming on Ni-based catalysts

	Reaction	A [a]	n	E [a]
1.	$H_2 + Ni(s) + Ni(s) \rightarrow H(s) + H(s)$	1.000×10^{-02} [b]	0.0	0.00
2.	$H(s) + H(s) \rightarrow Ni(s) + Ni(s) + H_2$	$5.593 \times 10^{+19}$	0.0	88.12
3.	$O_2 + Ni(s) + Ni(s) \rightarrow O(s) + O(s)$	1.000×10^{-02} [b]	0.0	0.00
4.	$O(s) + O(s) \rightarrow Ni(s) + Ni(s) + O_2$	$2.508 \times 10^{+23}$	0.0	470.39
5.	$CH_4 + Ni(s) \rightarrow CH_4(s)$	8.000×10^{-03} [b]	0.0	0.00
6.	$CH_4(s) \rightarrow Ni(s) + CH_4$	$5.302 \times 10^{+15}$	0.0	33.15
7.	$H_2O + Ni(s) \rightarrow H_2O(s)$	1.000×10^{-01} [b]	0.0	0.00
8.	$H_2O(s) \rightarrow Ni(s) + H_2O$	$4.579 \times 10^{+12}$	0.0	62.68
9.	$CO_2 + Ni(s) \rightarrow CO_2(s)$	1.000×10^{-05} [b]	0.0	0.00
10.	$CO_2(s) \rightarrow Ni(s) + CO_2$	$9.334 \times 10^{+07}$	0.0	28.80
11.	$CO + Ni(s) \rightarrow CO(s)$	5.000×10^{-01} [b]	0.0	0.00
12.	$CO(s) \rightarrow Ni(s) + CO$	$4.041 \times 10^{+11}$	0.0	112.85
		$\varepsilon_{CO(s)}$		−50.0 [c]
13.	$O(s) + H(s) \rightarrow OH(s) + Ni(s)$	$5.000 \times 10^{+22}$	0.0	97.90
14.	$OH(s) + Ni(s) \rightarrow O(s) + H(s)$	$2.005 \times 10^{+21}$	0.0	37.19
15.	$OH(s) + H(s) \rightarrow H_2O(s) + Ni(s)$	$3.000 \times 10^{+20}$	0.0	42.70
16.	$H_2O(s) + Ni(s) \rightarrow OH(s) + H(s)$	$2.175 \times 10^{+21}$	0.0	91.36
17.	$OH(s) + OH(s) \rightarrow O(s) + H_2O(s)$	$3.000 \times 10^{+21}$	0.0	100.00
18.	$O(s) + H_2O(s) \rightarrow OH(s) + OH(s)$	$5.423 \times 10^{+23}$	0.0	209.37
19.	$O(s) + C(s) \rightarrow CO(s) + Ni(s)$	$5.200 \times 10^{+23}$	0.0	148.10
20.	$CO(s) + Ni(s) \rightarrow O(s) + C(s)$	$1.418 \times 10^{+22}$	−3.0	115.97
		$\varepsilon_{CO(s)}$		−50.0 [c]
21.	$O(s) + CO(s) \rightarrow CO_2(s) + Ni(s)$	$2.000 \times 10^{+19}$	0.0	123.60
		$\varepsilon_{CO(s)}$		−50.0 [c]
22.	$CO_2(s) + Ni(s) \rightarrow O(s) + CO(s)$	$3.214 \times 10^{+23}$	−1.0	86.50
23.	$HCO(s) + Ni(s) \rightarrow CO(s) + H(s)$	$3.700 \times 10^{+21}$	0.0	0.0
		$\varepsilon_{CO(s)}$		50.0[c]
24.	$CO(s) + H(s) \rightarrow HCO(s) + Ni(s)$	$2.338 \times 10^{+20}$	−1.0	127.98
25.	$HCO(s) + Ni(s) \rightarrow O(s) + CH(s)$	$3.700 \times 10^{+24}$	−3.0	95.80
26.	$O(s) + CH(s) \rightarrow HCO(s) + Ni(s)$	$7.914 \times 10^{+20}$	0.0	114.22
27.	$CH_4(s) + Ni(s) \rightarrow CH_3(s) + H(s)$	$3.700 \times 10^{+21}$	0.0	57.70
28.	$CH_3(s) + H(s) \rightarrow CH_4(s) + Ni(s)$	$4.438 \times 10^{+21}$	0.0	58.83
29.	$CH_3(s) + Ni(s) \rightarrow CH_2(s) + H(s)$	$3.700 \times 10^{+24}$	0.0	100.00
30.	$CH_2(s) + H(s) \rightarrow CH_3(s) + Ni(s)$	$9.513 \times 10^{+22}$	0.0	52.58
31.	$CH_2(s) + Ni(s) \rightarrow CH(s) + H(s)$	$3.700 \times 10^{+24}$	0.0	97.10
32.	$CH(s) + H(s) \rightarrow CH_2(s) + Ni(s)$	$3.008 \times 10^{+24}$	0.0	76.43
33.	$CH(s) + Ni(s) \rightarrow C(s) + H(s)$	$3.700 \times 10^{+21}$	0.0	18.80
34.	$C(s) + H(s) \rightarrow CH(s) + Ni(s)$	$4.400 \times 10^{+22}$	0.0	160.49
35.	$O(s) + CH_4(s) \rightarrow CH_3(s) + OH(s)$	$1.700 \times 10^{+24}$	0.0	88.30
36.	$CH_3(s) + OH(s) \rightarrow O(s) + CH_4(s)$	$8.178 \times 10^{+22}$	0.0	28.72
37.	$O(s) + CH_3(s) \rightarrow CH_2(s) + OH(s)$	$3.700 \times 10^{+24}$	0.0	130.10
38.	$CH_2(s) + OH(s) \rightarrow O(s) + CH_3(s)$	$3.815 \times 10^{+21}$	0.0	21.97
39.	$O(s) + CH_2(s) \rightarrow CH(s) + OH(s)$	$3.700 \times 10^{+24}$	0.0	126.80
40.	$CH(s) + OH(s) \rightarrow O(s) + CH_2(s)$	$1.206 \times 10^{+23}$	0.0	45.42
41.	$O(s) + CH(s) \rightarrow C(s) + OH(s)$	$3.700 \times 10^{+21}$	0.0	48.10
42.	$C(s) + OH(s) \rightarrow O(s) + CH(s)$	$1.764 \times 10^{+21}$	0.0	129.08

[a] Arrhenius parameters for the rate constants written in the form: $k = AT^n \exp(-E/RT)$. The units of A are given in terms of moles, cm, and s. E is in kJ/mol.
[b] Sticking coefficient.
[c] Coverage-dependent activation energy (see Eq. (11)). Total available surface site density is $\Gamma = 2.60 \times 10^{-9}$ mol/cm^2.

Ni–YSZ anode.[1] This mechanism was initially developed and validated to describe steam-assisted catalytic partial oxidation of methane in small-channel monolith reactors using Ni supported on alumina. The 42 irreversible reactions involve 6 gas-phase and 12 surface-adsorbed species. Most reaction rates are represented in the Arrhenius form or as a sticking coefficient. However, the net activation energy of reactions 12, 20, 21, and 23 depend on the CO(s) coverage $\theta_{CO(s)}$ as [8]:

$$k = AT^n \exp\left(-\frac{E}{RT}\right) \exp\left(-\frac{\varepsilon_{CO(s)}\theta_{CO(s)}}{RT}\right). \quad (11)$$

The unity bond index-quadratic exponential potential (UBI-QEP) approach is used to determine the heats of adsorption, reaction enthalpies, and activation barriers for most relevant reactions [26–29]. In particular, the kinetic parameters for the desorption of O_2, CH_4, H_2O, CO_2 (reactions (4), (6), (8), and (10), respectively) [26], CO formation and decomposition (reactions (19) and (20)) [28], HCO reactions (reactions (23) and (24)) [26], and non-oxidative methane decomposition and formation (reactions (27)–(34)) [28] are based on this method. The water and CO_2 formation (reactions (13)–(18) and (21)–(22)), the second pathway for HCO formation (reactions (25) and (26)), and the oxidative decomposition and formation of CH_4 (reactions (35)–(42)) are also obtained from a theoretical study on CO_2 reforming of methane [29]. The sticking coefficient for hydrogen (reaction (1)) is taken from chemisorption studies on Ni(1 1 1) [30]. Hydrogen desorption (reaction (2)) is based on an experimental study on Ni single crystal surfaces [31]. Sticking coefficients for oxygen and water (reactions (3) and (7), respectively) are simply taken from studies on partial oxidation of methane over rhodium [17] due to a lack of data on Ni. The sticking coefficients for CH_4 and CO_2 adsorption (reactions (5) and (9), respectively) are derived from experimental studies of reforming and oxidation of methane over Ni-coated monoliths [32]. The data for CO adsorption/desorption (reactions (11) and (12)) on a vacant surface are taken from Al-Sarraf et al. [33].

Since the original kinetic data set is taken from a variety of different studies, the mechanism is a priori not thermodynamically consistent. Therefore, some of the original kinetic parameters were modified by an optimization procedure to ensure overall thermodynamic consistency regarding enthalpy and entropy. This methodology also permits the computation of the reverse rate coefficients, which depend on the forward rate coefficients and the thermodynamics [8].

Since the reaction mechanism is based on elementary molecular processes, it represents all the global processes in an SOFC anode, including (1) steam reforming of CH_4 to CO and H_2; (2) water–gas-shift processes; (3) surface-carbon coverage. Although the mechanism includes surface-adsorbed carbon C(s) and oxygen O(s) on the surface up to one monolayer, it has not been validated for conditions where coking and bulk-phase Ni oxidation occur. The experiments discussed in this paper are designed to operate under conditions where neither coking nor NiO formation occur. Practical fuel cells are also designed to operate under conditions that do not cause oxidation of the nickel or deposit formation. Nevertheless, there is value in extending reaction mechanisms to embody these effects. Such extended mechanisms would assist in design of cell architectures and operating conditions that avoid deleterious phenomena.

[1] The mechanism may be downloaded from http://www.detchem.com/mechanisms.

6. Results and discussion

A series of experiments are reported, seeking to understand and quantify steam and dry reforming within the anode. In these experiments the fuel-side flow is a mixture of forming gas and methane. The electrolyte side flow is a mixture of forming gas with various amounts of steam and carbon dioxide. Holding the channel inlet compositions fixed, the inlet flow rates are varied to alter the residence time in the channels. For the results reported here, the inlet flow rates in both channels are nominally the same. Generally speaking, the lower flow rates lead to longer residence times and more-complete reforming. However, even at the highest flow rates reported, there is still considerable reforming observed.

These experiments use flow rates that are high compared to flow rates in a typical fuel cell. With an objective of understanding the reforming kinetics, it is important to establish conditions where kinetics is important. At sufficiently low flow rates, there can be sufficient residence time that the chemistry within the anode may equilibrate. In this case, there is essentially no sensitivity to the kinetic pathways and rates.

In all cases, the measurements are compared with simulation results. The model does a very good job of representing the data, and certainly captures all the observed trends.

The results illustrated in Fig. 7 consider CO_2 introduced in electrolyte channel. Specifically, the inlet to the fuel channel is a mixture of 77.2% Ar, 2.8% H_2, and 20% CH_4. Inlet to the electrolyte channel is a mixture of 48.2% Ar, 1.8% H_2, and 50% CO_2. Inlet flow rates range from 50 to 150 sccm.

Both H_2 and CO are products of the reforming chemistry within the anode and are transported into both flow channels. As expected, increasing the channel flow rates decreases the CO and H_2 levels and increases the unreacted CO_2 and CH_4 levels. At higher flow rates, there is less time available for reaction and the products are more dilute in the flow channels. With CO_2 reforming, the CO levels are generally higher than H_2 levels. With steam reforming (discussed subsequently), the H_2 levels are higher. Although no steam is

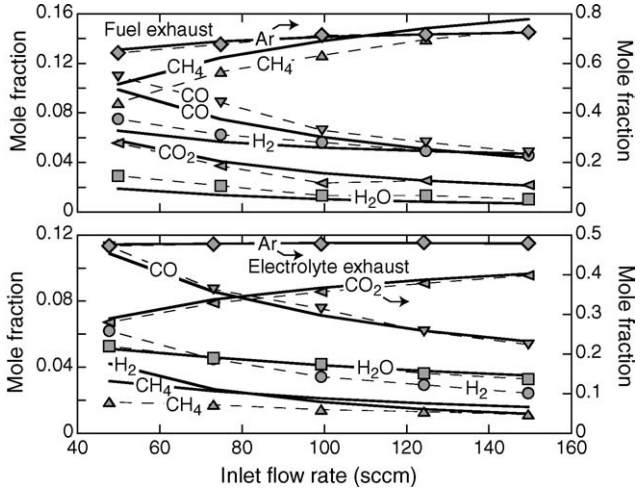

Fig. 7. Comparison of measurements (symbols) and model (solid lines) for dry reforming (CO_2) within the anode. Exhaust gas measurements for the fuel-side channel (upper panel) and the electrolyte-side channel (lower panel). Nominal inlet mole fractions to the fuel channel are $CH_4 = 0.20$, $H_2 = 0.028$, and $Ar = 0.772$. Nominal inlet mole fractions to the electrolyte channel are $CO_2 = 0.5$, $H_2 = 0.0175$, and $Ar = 0.4825$. The temperature is 800 °C and the pressure in both channels is 5000 Pa above atmospheric.

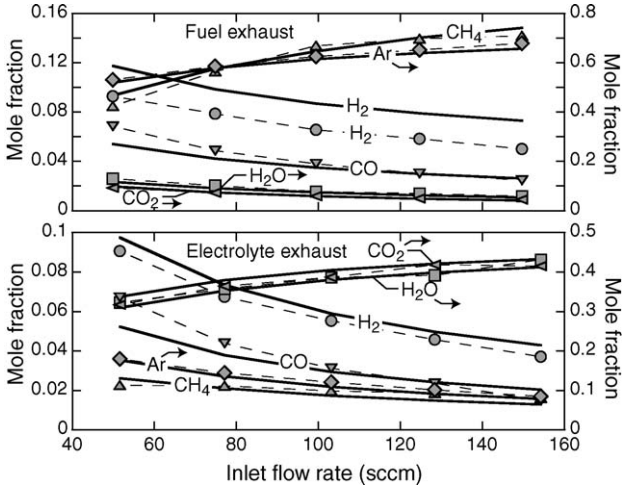

Fig. 9. Comparison of measurements (symbols) and model (solid lines) for mixed (CO_2/H_2O) reforming within the anode. Exhaust gas measurements for the fuel-side channel (upper panel) and the electrolyte-side channel (lower panel). Nominal inlet mole fractions to the fuel channel are $CH_4 = 0.2$, $H_2 = 0.028$, and $Ar = 0.772$. Nominal inlet mole fractions to the electrolyte channel are $H_2O = 0.5$ and $CO_2 = 0.5$. The temperature is 800 °C and the pressure in both channels is 5000 Pa above atmospheric.

introduced into the reactor, steam is a reaction product that can participate in the reforming process.

Fig. 8 shows a set of experiments where 50% steam is introduced into the electrolyte-side channel as the reforming agent. In this case H_2 is the dominant product of the reforming chemistry, with CO levels only reaching about one third of the H_2 levels. Low levels of CO_2 are also observed as a result of water–gas-shift processes. This CO_2 is available to participate as a dry-reforming reactant. Of all the cases reported here, the steam-reforming cases lead to the highest H_2 yields. As in all cases, higher channel flow rates lead to less reformate in the exhaust.

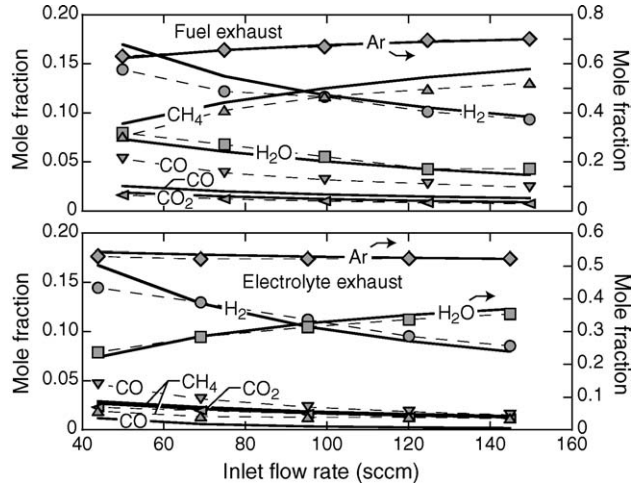

Fig. 8. Comparison of measurements (symbols) and model (solid lines) for steam (H_2O) reforming within the anode. Exhaust gas measurements for the fuel-side channel (upper panel) and the electrolyte-side channel (lower panel). Nominal inlet mole fractions to the fuel channel are $CH_4 = 0.20$, $H_2 = 0.028$, and $Ar = 0.772$. Nominal inlet mole fractions to the electrolyte channel are $H_2O = 0.48$, $H_2 = 0.018$, and $Ar = 0.502$. The temperature is 800 °C and the pressure in both channels is 5000 Pa above atmospheric.

Fig. 9 shows a set of experiments where a mixture of 50% steam and 50% CO_2 is introduced into the electrolyte-side channel as the reforming agent. As anticipated, the results lie between the steam and dry reforming cases.

As a check on the self-consistency of the measurements, element balances were evaluated for C, O, H, and Ar. Inlet mass-flow rates for each channel are controlled with mass-flow controllers and are known. However, since there is mass exchange between the channels through the porous anode, the exhaust mass-flow rates are not known for each channel. Although there are mass-flow controllers on the exhaust lines as part of the pressure-control system, they are not specifically calibrated for the exhaust-gas compositions. Therefore, model-predicted exhaust mass flow rates were used in estimating the element balances. The element balances were generally very good. For the dry-reforming cases (Fig. 7) the element balances closed to within about 2%. The steam-reforming cases (Fig. 8) had larger element imbalances averaging about 6%, with the O imbalance being about 15% at the lowest flow rates.

Perhaps the largest source of error in these experiments is the H_2O inlet flow rate. The partial pressure of steam coming out of the bubbler is highly sensitive to the bubbler temperature. A feedback control system maintains the bubbler temperature. Nevertheless, especially at high steam loadings around 50%, even a 2 °C temperature uncertainty leads to uncertainties in the steam loading of nearly 10%. Direct metering of H_2O by a syringe pump should reduce this uncertainty.

All the cases reported show comparable CH_4 consumption rates. This is consistent with the results reported by Wei

and Iglesia [24], showing that the steam- and dry reforming of methane on Ni-based catalysts proceed at similar rates. They attribute this similarity to the rate-limiting step being the first H-abstraction step in CH_4 on Ni, with the subsequent H-abstractions (ultimately forming surface carbon) being much faster. Comparing the rate coefficients of reactions (27), (29), (31), and (33) in Table 1 indicates similar kinetic behavior in this mechanism; the rate constant k_{27} is an order of magnitude smaller than any of the subsequent abstractions.

Over the entire range of conditions studied, the model represents the experimental observations well. Although there are many physical parameters in the model that could potentially be used as fitting parameters, all the parameters remain fixed for the simulations reported. The physical parameters for the porous 0.75 mm thick Ni–YSZ are: porosity $\phi = 0.35$, pore radius $r_p = 0.35\,\mu m$, particle diameter $d_p = 1.0\,\mu m$, and tortuosity $\tau = 4.5$. Although these parameters are not measured directly, they are certainly all quite reasonable. The specific area of catalyst surface is taken as $A_s = 5000\ cm^2/cm^3$. This value is consistent with the area that would be available for close-packed 1 μm diameter Ni spheres occupying 30% of the solid volume and with 30% of the Ni area being catalytically active. This area, which is difficult to estimate, was adjusted once to produce a good fit with the measurements for the mixed reforming case (Fig. 9) at the 100 sccm flow rate. Transport properties of the gases (e.g., viscosity and diffusion coefficients) are computed from kinetic theory with no adjustable parameters [8]. The rate constants in the heterogeneous reaction mechanism (Table 1) have not been adjusted in this work.

The experimental results are measured only at the channel exits. However, the models can provide much more information about the composition along the channel length and the local composition within the anode. Fig. 10 illustrates model results for the mixed CO_2–H_2O case at 100 sccm (Fig. 9). The top panel shows gas-phase species profiles along the length of the fuel channel, and the lower panel shows profiles along the electrolyte channel. The three panels in the middle show the predicted gas-phase profiles in the anode pore space and the surface-coverage profiles at three axial locations along the channels. Heterogeneous chemistry within the anode consumes the methane introduced in the fuel channel and the CO_2 and H_2O introduced in the electrolyte channel. There is net transport of CH_4 from the fuel channel toward the electrolyte channel and a net transport of CO_2 and H_2O from the electrolyte channel toward the fuel channel. There is also a net flow of Ar from the fuel channel toward the electrolyte channel. As the CH_4, CO_2, and H_2O mix within the anode pore space they react heterogeneously on the Ni surfaces. It is evident from the middle panels that H_2 and CO have maximum values within the anode where they are formed. They are transported diffusively and convectively (via the Dusty-Gas model) into both flow channels. Throughout the anode the Ni surfaces remain approximately 60% open. The surface coverages are dominated by adsorbed CO(s), H(s), and O(s).

The objective of the experiments and the modeling is to explore heterogeneous chemical-kinetic behavior within the

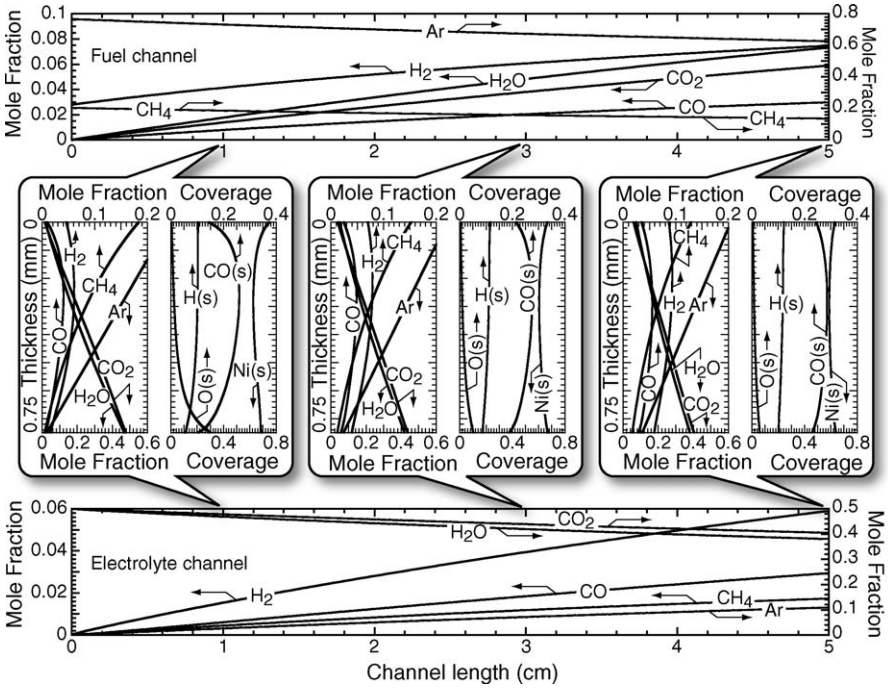

Fig. 10. Simulation predictions for mole-fraction profiles in the anode and electrolyte channels and for gas-phase mole fractions and surface coverage within the porous anode. Operating conditions are the same as in Fig. 9, with inlet flow rates of 100 sccm.

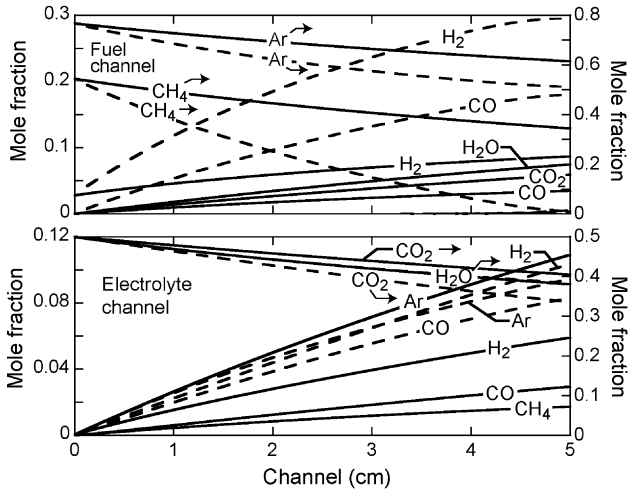

Fig. 11. Gas-phase mole-fraction profiles within the channels, comparing the effects of heterogeneous kinetics (solid lines) with assumed equilibrium (dashed lines) within the anode. Operating conditions are the same as in Fig. 9, with inlet flow rates of 100 sccm.

anode. Through the models, it is interesting to compare the limiting case of chemical equilibrium within the anode. A convenient method to simulate equilibrium within the anode pore space is to introduce two reversible global gas phase reactions that proceed at very high rates:

$$CH_4 + H_2O \rightleftharpoons 3H_2 + CO, \quad (12)$$

$$CO + H_2O \rightleftharpoons H_2 + CO_2. \quad (13)$$

Because these global reactions involve only gas phase species, the equilibrium constants are easily calculated from well known thermodynamic properties.

Fig. 11 shows the gas-phase compositions in the two channels for the same operating conditions as in Fig. 10. The solid lines show the same profiles as in Fig. 10 and the dashed lines show the solutions when the heterogeneous chemistry within the anode is equilibrated. Under these circumstances, it is immediately evident that the kinetics processes are rate-limiting. The kinetics simulations show very much slower consumption of CH_4 and production of CO and H_2. Inasmuch as the kinetics simulations agree well with the measurements, it is clear that heterogeneous kinetics play an important role. Thus, it is reasonable to assume that the experiments are run in regimes where valuable information about the kinetics can be determined.

Depending on operating conditions, flow rates in fuel-cell channels can be much lower than those in the experiments reported here. As flow rates decrease the residence times increase. At sufficiently low flow rates, the kinetics can run sufficiently fast as to approach equilibrium behavior. Although not reported in this paper, we apply the kinetics models in fuel-cell models. At relatively high cell voltages where the current density is relatively low, the kinetics tends toward equilibrium behavior. However, at low cell voltages, where current densities are high the reforming kinetics can be rate-limiting. The detailed kinetics models are general in the sense that they can predict the entire range of behavior from chemistry rate limitations to near-equilibrium behavior.

7. Summary and conclusions

The heterogeneous kinetics within porous Ni–YSZ anode structures has been studied using experiments and complementary models. The experiments are designed to measure the extent of reformation processes under conditions that are well away from chemical equilibrium. The model, which incorporates channel flow, convective and diffusive porous-media transport, and an elementary heterogeneous reaction mechanism, predicts the measured performance. Results are presented over a range of conditions that include pure steam reforming and pure CO_2 reforming as well as combination of the two. The understanding developed and the quantitative validation of the heterogeneous reaction mechanism can play an important role in the optimal design of anode structures for new solid-oxide fuel cells.

Acknowledgements

This work was supported by the DoD Multidisciplinary University Research Initiative (MURI) program administered by the Office of Naval Research under Grant N00014-02-1-0665. We are grateful to Dr. Paul Thoen of ITN Energy Systems for providing the Ni–YSZ anodes used in the experiments and to Prof. Neal Sullivan (Colorado School of Mines) for many helpful suggestions in developing the experiment.

References

[1] S. Singhal, K. Kendall, High-temperature Solid Oxide Fuel Cells: Fundamentals, Design and Applications, Elsevier Science Ltd, 2004.
[2] Fuel Cell Handbook (7th ed.), Tech. Rep. DOE/NETL 2004/1206, National Energy Technology Laboratory, Morgantown, WV, available at: http://www.netl.doe.gov (2004).
[3] Z. Zhan, J. Liu, S. Barnett, Appl. Catal. A 262 (2004) 255–259.
[4] F. Zhao, A. Virkar, J. Power Sources 141 (2005) 79–95.
[5] Y.-S. Chou, J. Stevenson, L. Chick, J. Power Sources 112 (2002) 130–161.
[6] H. Zhu, R. Kee, J. Power Sources 117 (2003) 61–74.
[7] K. Walters, A. Dean, H. Zhu, R. Kee, J. Power Sources 123 (2003) 182–189.
[8] R. Kee, M. Coltrin, P. Glarborg, Chemically Reacting Flow: Theory and Practice, Wiley, 2003.
[9] G. Gupta, E. Hecht, H. Zhu, A. Dean, R. Kee, J. Power Sources, in press.
[10] E. Mason, A. Malinauskas, Gas Transport in Porous Media: The Dusty-Gas Model, American Elsevier, New York, 1983.
[11] T. Thampan, S. Malhotra, H. Tang, R. Datta, J. Electrochem. Soc. 147 (2000) 3242–3250.
[12] T. Thampan, S. Malhotra, J. Zhang, R. Datta, Catal. Today 67 (2001) 15–32.

[13] R. Kee, G. Dixon-Lewis, J. Warnatz, M. Coltrin, J. Miller, A Fortran computer code package for the evaluation of gas-phase multicomponent transport properties, Tech. Rep. SAND 86–8246, Sandia National Laboratories, 1986.
[14] D. Goodwin, in: M. Allendorf, F. Maury, F. Teyssandier (Eds.), Chemical Vapor Deposition XVI and EUROCVD 14, vol. PV 2003–08, Electrochemical Society, 2003, pp. 155–162, see also http://www.cantera.org.
[15] J. Bear, Dynamics of Fluids in Porous Media, American Elsevier, New York, 1972.
[16] D. Chatterjee, O. Deutschmann, J. Warnatz, Faraday Discuss. 119 (2001) 371–384.
[17] R. Schwiedernoch, S. Tischer, C. Correa, O. Deutschmann, Chem. Eng. Sci. 58 (2003) 633–642.
[18] D. Zerkle, M. Allendorf, M. Wolf, O. Deutschmann, J. Catal. 196 (2000) 18–39.
[19] M. Bradford, M. Vannice, Catal. Rev. Sci. Eng. 41 (1999) 1–42.
[20] J. Xu, G. Froment, AIChE J. 35 (1989) 88–96.
[21] J. Rostrup-Nielsen, J. Anderson, M. Boudart, CATALYSIS—Science and Technology, vol. 5, Springer, 1984.
[22] D. Chen, R. Lodeng, A. Anundskas, O. Olsvik, A. Holmen, Chem. Eng. Sci. 56 (2001) 1371–1379.
[23] L. Aparicio, J. Catal. 165 (1997) 262–273.
[24] J. Wei, E. Iglesia, J. Catal. 224 (2004) 370–383.
[25] J. Zhu, J. van Ommen, L. Lefferts, J. Catal. 225 (2004) 388–397.
[26] E. Shustorovich, Adv. Catal. 37 (1990) 101–163.
[27] E. Shustorovich, H. Sellers, Surf. Sci. Rep. 31 (1998) 1–119.
[28] A. Bell, E. Shustorovich, Metal Surface Reaction Energetics: Theory and Application to Heterogeneous Catalysis, Chemisorption and Surface Diffusion, Wiley, 1991 (Chapter 5).
[29] M. Hei, H. Chen, J. Yi, Y. Lin, Y. Lin, G. Wei, D. Liao, Surf. Sci. 417 (1998) 82–96.
[30] J. Lapujoulade, K. Neil, J. Chem. Phys. 57 (1972) 3535–3545.
[31] K. Christmann, O. Schober, G. Ertl, M. Neumann, J. Chem. Phys. 60 (1974) 4528–4540.
[32] B. Schädel, Untersuchung von Reformierungsprozessen von Methan an Rhodium- und Nickelkatalysatoren, Master's Thesis, Department of Chemistry and Biosciences, University of Karlsruhe, 2004.
[33] N. Al-Sarraf, J. Stuckless, C. Wartnaby, D. King, Surf. Sci. 283 (1993) 427–437.